Horizontal and vertical dispersion in a wind-driven oceanic gyre model

J. R. Barrientos Valencia,[1] L. Zavala Sansón*,[1] and F. J. Beron-Vera[2]

[1)]*Departamento de Oceanografía Física, CICESE, Ensenada 22860, México*

[2)]*Department of Atmospheric Sciences, Rosenstiel School of Marine, Atmospheric, and Earth Science, University of Miami, Miami FL, USA*

(*Author to whom correspondence should be addressed: lzavala@cicese.mx)

(Dated: 11 September 2024)

This study addresses the horizontal and vertical dispersion of passive tracers in idealized wind-driven subtropical gyres. Synthetic particles within a closed basin are numerically advected to analyze their dispersion under different theoretical velocity fields. Horizontal dispersion simulations incorporate the classic wind-driven Stommel circulation along with (i) surface Ekman drift associated with the Stommel wind field and (ii) inertial effects due to particle size and buoyancy. Results reveal that the Ekman drift inhibits particle dispersion across the entire domain leading to tracer concentration in a quasi-stable distribution skewed towards the western side of the basin. Similar behavior is observed with inertial particles. The equilibrium state is quantified for different diffusivity values, particle sizes and buoyancies. For vertical dispersion, simulations incorporate the three-dimensional Ekman velocity, which includes a negative vertical component, while ignoring inertial effects. Initially, surface particles accumulate around the gyre center while slowly sinking, but they disperse across the basin once they surpass the Ekman layer and are free from surface effects. Tracers sink more on the western side of the basin, regardless of horizontal diffusivity. On average, ignoring inertial effects, particles sink less with higher diffusivity and more with lower diffusivity, suggesting a potential for high horizontal distribution of sunken tracers in the ocean.

Dispersion in a wind-driven oceanic model

I. INTRODUCTION

The study of organic and synthetic matter dispersion in the ocean is essential for addressing critical environmental questions. These include understanding the impact on ecosystems, the distribution of nutrients (McGillicuddy Jr, 2016), the dispersal of macroalgae such as *Sargassum* (Beron-Vera et al., 2022), and the general behavior of floating and sinking material (Jambeck et al., 2015). In particular, monitoring large-scale floating debris (Miron et al., 2020), mainly plastic, represents one of the most significant problems due to its impact on marine ecosystems (van der Mheen et al., 2019; Amador González and Zavala Sansón, 2023).

In general, analyzing the transport and diffusion mechanisms in the ocean is a difficult task because of the highly turbulent character of oceanic motions; that is, the interaction of phenomena at a great variety of different temporal and spatial scales that range from 1 mm to 10^4 km. Some dispersion phenomena occur on the first meters of the upper ocean. For instance, a significant proportion of floating material is accumulated on the surface of subtropical convergence regions around the world's oceans, known as garbage patches (van Sebille et al., 2012; Maximenko et al., 2012). Numerous studies have addressed the formation mechanisms of these accumulation areas, but there are still several open issues, some of which will be examined here.

The problem of horizontal ocean dispersion has been extensively studied from a Lagrangian point of view in the last decades. Horizontal dispersion models are often based on physical principles to incorporate representative ocean circulations, such as Stommel-like flows for subtropical gyres in large-scale and regional basins, Ekman dynamics due to wind effects on the ocean surface, and Stokes drift generated by ocean waves. With this information, a large number of particles are advected, and their evolution in time and space is analyzed to quantify dispersion (Kubota, 1994; Richards et al., 1995; Buffoni et al., 1997; Berloff et al., 2002; Durán Colmenares and Zavala Sansón, 2022). Other studies consider the particles' characteristics, such as their size and buoyancy, which allows studying inertial effects that lead to different accumulation processes (Beron-Vera et al., 2016, 2019). Another approach applies statistical methods based on transition probabilities calculated from historical buoy trajectories on the ocean surface (Maximenko et al., 2012; Onink et al., 2019; Amador González and Zavala Sansón, 2023). These studies report large accumulation zones in the subtropical gyres of both hemispheres. The main physical driving forces are the Ekman drift dynamics (van Sebille et al., 2012) and inertial effects (Beron-Vera et al., 2016), although their relative importance still needs to be clarified. A great source of un-

certainty in physical dispersion models is the difficulty in elucidating the role of diffusive effects in oceanic conditions. This problem is often attacked by employing stochastic models, in which Lagrangian particles are subject to the action of random impulses that, on average, are designed to represent dispersion processes associated with the action of turbulent eddies (Griffa, 1996; Berloff and McWilliams, 2002; Ocampo Jaimes et al., 2022).

Another fundamental problem concerns three-dimensional dispersion when the wind induces significant vertical motions (such as Ekman pumping), or exerts a direct action on objects due to their properties (weight, form, size). The main interest regarding vertical dispersion is the fate of sinking material in the open ocean (Cózar et al., 2014) and coastal regions (Jalón-Rojas et al., 2019). The problem of vertical dispersion and its effects on horizontal dispersion is vastly unknown because of the difficulty of measuring concentrations or collecting water samples at different depths in large-scale regions and during prolonged periods. Consequently, the problem has been mainly approached from a modeling perspective. For instance, the spreading of tracers and horizontal dispersion at the deep ocean has been calculated in idealized double-gyre Stommel flows (Berloff et al., 2002; Berloff and McWilliams, 2002). At smaller scales, vertical dispersion has been studied through high-resolution numerical modeling ($\sim$ 1 km), which has demonstrated the ability of submesoscale and mesoscale vortices to disperse particles vertically in eddy-dominated currents (Zhong and Bracco, 2013; Zhong et al., 2017).

The Ekman dynamics forced by the wind within the relatively thin boundary layer at the ocean-air interphase (a few tenths of m) play a relevant role in generating vertical motions. In particular, the Ekman pumping, associated with convergence and divergence in the Ekman layer, is one of the primary mechanisms that can sink (or raise) passive fluid or material from (to) the surface. From large-scale numerical simulations, it is found that upwelling occurs mainly in the equatorial zone, while the subsidence regions are closely related to the litter patches in the subtropical gyres (Froyland et al., 2014). At the mesoscale, Ekman pumping can influence the evolution of cyclonic and anticyclonic eddies (Zavala Sansón et al., 2023), and the distribution of tracers (for example, nutrients and chlorophyll) within these structures (Estrada-Allis et al., 2019).

In this study, we use a Lagrangian description to analyze the trajectories of individual particles subject to the action of different dispersive mechanisms in an idealized large-scale flow and calculate statistical metrics for horizontal and vertical dispersion. The main procedure consists of performing numerical simulations of many particles in a closed basin to analyze their dispersion due to different velocity fields. Specifically, we consider

1. the classical wind-driven Stommel circulation,
2. the Ekman velocity associated with the Stommel wind field,
3. inertial effects (due to the particle size and buoyancy), and
4. turbulent diffusive effects simulated with a stochastic model.

The aim is to determine the horizontal and vertical dispersion due to these mechanisms separately or together and their relative importance. Our approach is based on relatively simple analytical models because the results provide new light on the individual and collective action of different physical agents.

To study horizontal dispersion, we consider the particle advection in different Stommel gyres, including the resulting surface Ekman drift. The results are presented for different diffusive effects measured with a suitable Péclet number. In agreement with previous studies (Maximenko et al., 2012; van Sebille et al., 2012), surface Ekman drift forces particles to converge toward a region around the centre of the Stommel gyre. However, this convergence depends on the turbulent diffusion. For sufficiently small diffusivity, the Ekman convergence can prevent filling the whole domain as observed in the purely Stommel problem (Richards et al., 1995). Furthermore, inertial effects, associated with the particle size and buoyancy, cause a greater convergence than that produced by the Ekman drift, as discussed previously by Beron-Vera et al. (2016). These findings support the notion that garbage patches in subtropical gyres might be more influenced by the inertial properties of floating particles than the traditional Ekman mechanism usually invoked in past studies.

Regarding vertical dispersion, we investigate sinking particles using the three-dimensional Ekman velocity in a Stommel gyre. The aim is to obtain an estimate of the vertical distribution of the tracers as well as their evolution over time. Also, the impact of vertical motions in the large-scale horizontal distribution is analyzed. In particular, we examine the effects of horizontal diffusivity on the long-term depth reached by sinking tracers initially released at the surface. For instance, low horizontal diffusivity promotes tracers to reach greater depths because they remain longer in regions of more significant subsidence. The results show that more particles sink at the western side of the basin, near the gyre center. The obtained horizontal particle distributions at different depths suggest a possible configuration of sinking material in the ocean, which remains a topic of hot debate (Isobe and Iwasaki, 2022).

The content of the article is arranged as follows. Sec. II describes the models used as well as the configuration of the simulations. The results on horizontal and vertical dispersion are shown in Sec. III and IV, respectively. The conclusions are presented in Sec. V. Finally, the Appendix summarizes in more detail the model for inertial particles proposed by Beron-Vera et al. (2019).

II. PHYSICAL MODELS

Our main goal is to study horizontal and vertical particle dispersion in a Stommel gyre and in the presence of Ekman or inertial effects. In Sec. II A, we provide a short description of these deterministic flow models, and in Sec. II B we present the stochastic method to simulate turbulent diffusion. The design of the experiments is explained in Sec. II C.

A. Deterministic flow models

1. Stommel model

The Stommel (1948) model is an idealized description of large-scale subtropical gyres in a homogeneous ocean in a mid-latitude rectangular basin. The model explains the western-intensified anticyclonic circulation driven by a negative-curl zonal wind in the presence of linear bottom friction. Here, we assume a square basin of length L and depth H in a Cartesian system with horizontal coordinates (x,y) pointing eastward and northward, respectively. The origin is the southwest corner. The stationary, linear vorticity equation is

$$\beta \frac{\partial \psi}{\partial x} = \frac{1}{\rho_O H} \left(\nabla \times \boldsymbol{\tau}\right)_z - s\nabla^2 \psi, \tag{1}$$

where $\psi(x,y)$ is the stream function, ρ_O the water density, $\boldsymbol{\tau} = (\tau_x, \tau_y)$ the surface wind-stress vector, s the friction parameter (with units of 1/time), and β the latitudinal gradient of the Coriolis parameter. The single-gyre Stommel solutions are built with a simplified representation of the effect of the trade winds in the southern part and counter-trade winds in the northern side of the basin, which generate the wind stress $\boldsymbol{\tau}$ and its curl defined as

$$\boldsymbol{\tau} = \left(-\tau_0 \cos\left(\frac{\pi y}{L}\right), 0\right), \qquad \left(\nabla \times \boldsymbol{\tau}\right)_z = -\frac{\tau_0 \pi}{L} \sin\left(\frac{\pi y}{L}\right). \tag{2}$$

This form of the surface stress only depends on the latitudinal position y.

The Stommel stream function is

$$\psi(x,y) = -A\left[1 - m_3 e^{m_1 x/L} - (1-m_3)e^{m_2 x/L}\right]\sin\left(\frac{\pi y}{L}\right), \tag{3}$$

where the constants are

$$A = \frac{\tau_0 L}{\rho_O H \pi s}, \qquad \varepsilon = \frac{s}{\beta L} \equiv \frac{\ell}{L}, \tag{4}$$

$$m_1 = \frac{-\varepsilon^{-1} + \sqrt{\varepsilon^{-2} + 4\pi^2}}{2}, \qquad m_2 = \frac{-\varepsilon^{-1} - \sqrt{\varepsilon^{-2} + 4\pi^2}}{2}, \qquad m_3 = \frac{1 - e^{m_2}}{e^{m_1} - e^{m_2}}. \tag{5}$$

The parameter ε represents the thickness of the western boundary layer, $\ell = s/\beta$, divided by the basin width L. The horizontal velocity components are

$$\boldsymbol{u_G} = (u_G, v_G) = \left(\frac{\partial \psi}{\partial y}, -\frac{\partial \psi}{\partial x}\right). \tag{6}$$

The maximum speed is found on the western border, at $(x/L, y/L = (0, 0.5)$. The recirculation flow at the eastern side of the gyre has a velocity scale $U_0 = |\psi|_{max}/L$, where $|\psi|_{max}$ is the maximum stream function in absolute value at the centre of the gyre (Richards et al., 1995). For our purposes, we define a Stommel flow with ε and U_0. Figure 1 shows the streamlines of three Stommel gyres with different ε and U_0. The plots also show that the zonal distance d_{max} between the gyre and basin centres (which will be helpful later) decreases with ε. This distance is defined as

$$d_{max} = L/2 - x_G, \tag{7}$$

where x_G is the zonal position of the gyre centre. Using solution (3), it is found that

$$x_G = \frac{L}{m_1 - m_2} \log\left[\frac{(m_3 - 1)m_2}{m_3 m_1}\right], \tag{8}$$

where constants m_1, m_2 and m_3, given in (5) depend on ε. It can be verified that $x_G \to L/2$ for large ε (e.g. for very small β), so d_{max} tends to zero in that limit.

2. Ekman velocity

To study horizontal dispersion at the ocean surface, we use the Ekman drift. Later, when examining vertical dispersion, we consider the resulting vertical velocity or Ekman pumping.

Ekman drift. The surface boundary layer of the ocean is the Ekman layer generated by the wind stress. Within this layer, the predominant balance is between the Coriolis terms, the pressure

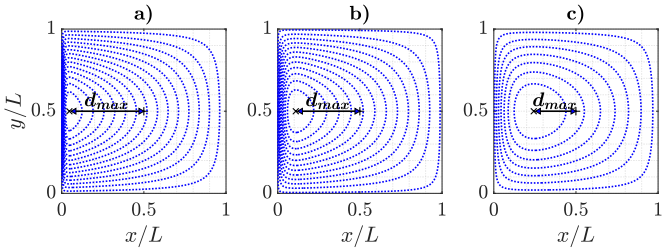

FIG. 1: Stream function contours of Stommel gyres $\psi(x,y)$. (a) $\varepsilon = 0.01$, $U_0 = 0.033$ m/s. (b) $\varepsilon = 0.03$, $U_0 = 0.027$ m/s. (c) $\varepsilon = 0.1$, $U_0 = 0.017$ m/s. In all cases, $L = 2000$ km and the contour interval is 4500 m^2/s. The amplitudes A are calculated from (4) for each ε and using $\tau_0 = 0.2$ N/m^2, $H = 500$ m, $\rho_O = 1035$ Kg/m^3, $\beta = 1.7 \times 10^{-11}$ (m s)$^{-1}$. The distance between the gyre and basin centres is defined as d_{max}.

gradients and vertical viscous effects. Setting the origin of the vertical coordinate $z = 0$ at the surface, the horizontal Ekman flow for arbitrary surface stress is

$$u_E = \frac{\sqrt{2}}{\rho_O f_0 d} e^{z/d} \left[\tau^x \cos\left(\frac{z}{d} - \frac{\pi}{4}\right) - \tau^y \sin\left(\frac{z}{d} - \frac{\pi}{4}\right) \right], \tag{9}$$

$$v_E = \frac{\sqrt{2}}{\rho_O f_0 d} e^{z/d} \left[\tau^x \sin\left(\frac{z}{d} - \frac{\pi}{4}\right) + \tau^y \cos\left(\frac{z}{d} - \frac{\pi}{4}\right) \right], \tag{10}$$

where d is the vertical scale of the boundary layer and f_0 the Coriolis parameter at a reference latitude (Cushman-Roisin and Beckers, 2009). Within the Ekman layer ($|z| < d$) the direction of the flow changes clockwise (in the northern hemisphere) generating the well-known Ekman spiral.

The Ekman drift is defined as the surface current at $z = 0$. The resulting velocity is rotated an angle $\pi/4$ to the right of the wind. The Ekman drift due to the zonal stress of the Stommel wind (2) is

$$\boldsymbol{u_D} = u_D \cos\left(\frac{\pi y}{L}\right)(-1, 1), \tag{11}$$

where $u_D = \tau_0/(\rho_O f_0 d)$ is the magnitude. Typical values are $u_D \approx 0.1$ m/s or less (here, we will this value in all experiments). For a recent discussion on the role of Ekman currents in surface transport, see Onink et al. (2019).

Ekman pumping. To sink particles, we consider the vertical motions due to the flow divergence in the surface boundary layer. The resulting vertical velocity component w_E is known as

Ekman pumping. Integrating the continuity equation $\nabla\cdot(u_E,v_E,w_E)$ from an arbitrary depth $z<0$ to the surface at $z=0$, yields

$$\int_z^0 \partial_{z'} w_E(x,y,z')\,dz' = w_E(x,y,0) - w_E(x,y,z) = -\int_z^0 (\partial_x u_E + \partial_y v_E)\,dz'. \tag{12}$$

Assuming $w_E(x,y,0)=0$ (i.e. ignoring free-surface effects) and using (9)-(10), the Ekman vertical velocity is

$$w_E(x,y,z) = \frac{1}{\rho_O f_0}\left\{(\nabla\times\boldsymbol{\tau})_z - e^{z/d}\left[\nabla\cdot\boldsymbol{\tau}\,\sin\left(\frac{z}{d}\right) + (\nabla\times\boldsymbol{\tau})_z\cos\left(\frac{z}{d}\right)\right]\right\}. \tag{13}$$

When $|z|\gg d$, we obtain the linear Ekman pumping between the Ekman layer and the geostrophic interior, commonly used for meso- and large scale geophysical flows (see e.g. Cushman-Roisin and Beckers, 2009)

$$w_E(x,y,z\to-\infty) = \frac{1}{\rho_O f_0}(\nabla\times\boldsymbol{\tau})_z. \tag{14}$$

From the Ekman components (9), (10) and (13), the three-dimensional Ekman velocity for arbitrary surface stress $\boldsymbol{\tau}$ is

$$\boldsymbol{u_E} = (u_E, v_E, w_E). \tag{15}$$

Using the Stommel forcing, its curl (2), and $\nabla\cdot\boldsymbol{\tau}=0$, the Ekman components are

$$u_E(y,z) = -u_D\, e^{z/d}\cos\left(\frac{\pi y}{L}\right)\cos\left(\frac{z}{d}-\frac{\pi}{4}\right), \tag{16}$$

$$v_E(y,z) = -u_D\, e^{z/d}\cos\left(\frac{\pi y}{L}\right)\sin\left(\frac{z}{d}-\frac{\pi}{4}\right), \tag{17}$$

$$w_E(y,z) = \frac{\pi d}{L}u_D\sin\left(\frac{\pi y}{L}\right)\left[e^{z/d}\cos\left(\frac{z}{d}\right)-1\right]. \tag{18}$$

Note that these fields only depend on y and z. The vertical velocity is negative (due to the negative stress curl) and much smaller than the horizontal components because $d\ll L$. Also, w_E is very small near the surface, $|z|<d$; then increases with depth until reaching a constant value, the Ekman pumping

$$w_E(y,|z|\gg d) = -\frac{\pi d}{L}u_D\sin\left(\frac{\pi y}{L}\right). \tag{19}$$

The maximum pumping values are along the middle latitude, $y=L/2$, and are zero at the zonal walls, $y=0,L$. The horizontal components become negligible outside the boundary layer.

3. *Inertial effects*

The inertial model considers particles that have a finite size and density different from that of water. To analyze the behaviour of inertial particles, Maxey and Riley (1983) developed equations of motion for small rigid spheres carried by a flow. From these equations, Beron-Vera et al. (2019) extended the model to consider the effects of both the ocean current and the wind drag by assuming that the tracers are partially floating on the surface. What follows is a summary of the equations with the relevant variables and approximations.

The model consists of partially floating spherical particles in the air-water interface at $z = 0$. The formulation includes the water density ρ_O, the air density $\rho_A \ll \rho_O$, and the corresponding dynamic viscosity coefficients μ_O and μ_A. The drag exerted by wind and water on the particle is introduced through Stokes' law and integrated over the sunken portion and the portion exposed to the wind. The model also includes Coriolis effects. The fundamental parameters are the radius of the spheres r and the buoyancy

$$\delta \equiv \frac{\rho_O}{\rho_p} \geq 1, \tag{20}$$

where ρ_p is the particle density and ρ_O is the density of seawater. Note that $\delta = 1$ means a completely sunken sphere, and $\delta > 1$ is a partially floating sphere. The upper limit is bounded to values of $O(1) \gtrsim 1$, as discussed by Olascoaga et al. (2020), who performed experiments using drifting buoys with buoyancy values not exceeding $\delta = 4$, approximately. Furthermore, the particles' radius is assumed to be sufficiently small, so they respond quickly to the drag exerted by the water and air, i.e., the Stokes relaxation time is very short.

Ocean currents and wind are defined by the velocity vectors $\boldsymbol{u_O}(\boldsymbol{x},t)$ and $\boldsymbol{u_A}(\boldsymbol{x},t)$, respectively (with $\boldsymbol{x}$ the two-dimensional position vector). If the ocean currents are nearly geostrophic and the winds are calm, the velocity of a sufficiently small particle floating at the ocean surface is asymptotically, i.e., in the long run, given by

$$\boldsymbol{v_p} = (1-\alpha)\boldsymbol{u_O} + \alpha \boldsymbol{u_A} + \tau_s f_0 \left(-(1-\alpha-R)\boldsymbol{u_O^\perp} - \alpha \boldsymbol{u_A^\perp}\right), \tag{21}$$

where $\boldsymbol{u_O^\perp}$ and $\boldsymbol{u_A^\perp}$ are the corresponding perpendicular velocity vectors (rotated $\pi/2$ to the left). The dimensionless constants R, α, and the generalized Stokes time τ_s depend on two or more of the parameters of the problem $(r, \delta, \rho_O, \mu_O, \mu_A)$. The explicit expressions of the three constants are presented in the Appendix. In all experiments we use $f_0 = 9.4 \times 10^{-5}$.

For simplicity, we assume that the wind velocity $\boldsymbol{u_A}$ has a behavior identical to the wind stress

(2) defined in the Stommel model (thus avoiding the use of a bulk formula and additional parameters, e.g., a drag coefficient). Thus, the wind only depends on the latitudinal position as

$$\boldsymbol{u_A} = -u_A \left(\cos\left(\frac{\pi y}{L_y}\right), 0 \right), \tag{22}$$

where u_A is the magnitude. In addition, the ocean currents are due to the Stommel circulation, that is, $\boldsymbol{u_O} = \boldsymbol{u_G}$. Thus, we can rewrite (21) as

$$\boldsymbol{v_p} = \boldsymbol{u_G} + \boldsymbol{u_I}, \tag{23}$$

where the inertial velocity $\boldsymbol{u_I}$ is defined as

$$\boldsymbol{u_I} = \alpha(\boldsymbol{u_A} - \boldsymbol{u_G}) + \tau_s f_0 \left(-(1-\alpha-R)\boldsymbol{u_G^\perp} - \alpha \boldsymbol{u_A^\perp} \right). \tag{24}$$

This velocity field incorporates inertial effects modulated by the parameters r and δ in a geostrophic Stommel flow and the corresponding wind field. The contribution of the Ekman velocity is added independently of the inertial effects.

B. Stochastic model and Lagrangian metrics

1. Turbulent diffusion in a random walk model

Consider N particles in the basin with positions $\boldsymbol{x_i}$ where $i = 1, \ldots, N$. Particle motions are followed by solving the stochastic trajectory equations in differential form

$$d\boldsymbol{x_i} = \boldsymbol{u_i}(\boldsymbol{x_i}, t)dt + \boldsymbol{u}_a(t)dt, \tag{25}$$

where $\boldsymbol{u_i}(\boldsymbol{x}, t)$ is the deterministic velocity of the particle imprinted by the Stommel wind-driven circulation, the Ekman velocity, and/or inertial effects, dt is the time increment, and $\boldsymbol{u}_a$ a horizontal stochastic term representing the turbulent velocity that generates horizontal diffusion (Graef et al., 2020). Since the spatial and temporal scales of the turbulent velocity are much smaller than the advective effects of the deterministic flows, their effects can be parameterized with a constant eddy-diffusivity coefficient (Griffa, 1996). At each discrete time step $\Delta t \equiv dt$, the particles move at a constant speed u_a in a random direction $\Theta_i(t) \in [0, 2\pi]$, independent of its previous displacement and the other particles (Markov process). The random velocity with constant magnitude and variable direction for each particle is

$$\boldsymbol{u}_a = u_a \left(\cos\Theta_i(t), \sin\Theta_i(t) \right). \tag{26}$$

The advection scheme to solve the deterministic part of (25) is a standard fourth-order Runge-Kutta scheme. Then, the stochastic perturbation is added at each step as a displacement $u_a \Delta t$ in a random direction, which does not depend on the flow carrying the particle. The horizontal diffusivity generated by the stochastic process is

$$\kappa = \frac{1}{2} u_a^2 \Delta t. \tag{27}$$

It is estimated that the horizontal diffusivity in large oceanic scales ranges from 100 $\mathrm{m^2 s^{-1}}$ to 1000 $\mathrm{m^2 s^{-1}}$ (Griffa, 1996). In this work, different values are considered, from the modest diffusivity of 100 $\mathrm{m^2 s^{-1}}$ to an overestimation of 2000 $\mathrm{m^2 s^{-1}}$ to compare the resulting particle distribution and its consequences.

2. *Lagrangian statistics in a closed box*

The normalised square domain (using the side-length L) is defined by the rectangular coordinates $0 \leq x \leq 1$, $0 \leq y \leq 1$, and $z \leq 0$. The ocean surface is at $z = 0$. In the simulations of horizontal dispersion, a large number of particles were initialized in a given location (point charges) at the surface. In experiments of vertical dispersion, the particles were initialized at a single point or were randomly distributed at a predetermined z level. Further details are given in the corresponding sections. To simulate a closed basin and to prevent particles from escaping due to the large-scale flow or a stochastic fluctuation, the boundary condition consists of elastic collisions satisfying the conservation of linear momentum. Then, upon colliding with the wall, the tracer must reverse the direction of the velocity component perpendicular to the boundary but maintain the original speed; the tangential velocity is not modified after the collision (Zavala Sansón et al., 1998).

To quantify the horizontal spread of particles from a point source, we use classical metrics based on two-particle statistics, which describe the evolution of the cloud of particles as they are dispersed (Csanady, 2012; Zavala Sansón et al., 2017; Flores Ramírez and Zavala Sansón, 2019). The horizontal relative dispersion of particle pairs is defined as

$$D^2(t) = D_x^2(t) + D_y^2(t), \tag{28}$$

where D_x^2 and D_y^2 are the mean quadratic separation between particle pairs in the x and y directions, respectively. For N particles there are $N(N-1)/2$ pairs and then, for instance, the x component is

$$D_x^2(t) = \frac{2}{N(N-1)} \sum_{p<q} [x_p(t) - x_q(t)]^2. \tag{29}$$

The expression for D_y^2 is analogous. Similarly, one can define the vertical dispersion D_z^2 with the z-positions.

As tracers disperse by diffusive effects, they fill the basin, so the dispersion reaches a maximum value (corresponding to a uniform distribution over the whole domain). For a square basin of length L, the maximum dispersion values are (Flores Ramírez and Zavala Sansón, 2019)

$$D_{max}^2 = \frac{L^2}{3}, \qquad (D_x^2)_{max} = (D_y^2)_{max} = \frac{L^2}{6}. \tag{30}$$

The particles will also fill the domain when adding a non-divergent deterministic flow, as in the Stommel circulation (Richards et al., 1995). We shall examine examples where the dispersion reaches the maximum value and cases where a convergent flow accumulates particles, preventing the dispersion from reaching D_{max}^2.

For cases in which there is vertical displacement of the tracers, we calculate the absolute dispersion from their initial position as

$$A_z^2(t) = \frac{1}{N}\sum_{i=1}^{N}[z_i(t) - z_i(t_0)]^2, \tag{31}$$

where $z_i^p(t)$ is the vertical position of the i-th particle and t_0 is the initial time.

C. Design of the experiments

1. Advection and diffusion

Given a Stommel flow whose strength is given by U_0, the advective and diffusive time scales are

$$T = \frac{L}{U_0}, \qquad T_d = \frac{L^2}{\kappa}, \tag{32}$$

respectively. The advective scale represents the time a particle takes to turn around the whole domain, starting from an intermediate streamline. The advection-diffusion effects are measured with the Péclet number

$$Pe \equiv \frac{T_d}{T} = \frac{U_0 L}{\kappa}. \tag{33}$$

In meso and large-scale oceanic conditions, it is usually found that $Pe >> 1$, so the advective time is shorter than the diffusive time. However, the effective diffusion also depends on the structure of the Stommel flow determined by U_0 and ε (Young, 1984). According to this view, the time scale for mixing a tracer depends on the dispersion regime determined by the Stommel gyre and

the Péclet number. There is the "weakly diffusive limit", in which $\varepsilon Pe \gg 1$, and the "strongly diffusive limit" when $\varepsilon Pe \ll 1$. The transition occurs for $\varepsilon Pe \sim 1$. The dispersion in our experiments is between the weak and the transition diffusive regimes. The time scale for mixing defined by Young (1984) is

$$T_\ell = \frac{\varepsilon L^2}{\kappa}, \tag{34}$$

which will refer to as the Young time. Richards et al. (1995) proposed modifying this time scale by including the length of the streamline along the boundary layer; however, that refinement will not be considered here.

2. *Flow parameters and overall organization*

Table I shows ε, U_0 and T (columns 1 to 3) for three different Stommel flows used in our simulations. The corresponding Young time scales T_ℓ are shown in columns 4 and 5 for the lowest and highest diffusivity cases (simulations with intermediate values were also performed). The Péclet numbers are shown in columns 6 and 7. The duration of the simulations was arbitrary depending on the case to be studied, but the minimum period was T_ℓ (of order of several years). The position of the particles was calculated with a time step $\Delta t = 1.5$ days, which was adequate for the Runge-Kutta method.

ε	U_0 (m/s)	$T = L/U_0$ (y)	$T_\ell = \varepsilon L^2/\kappa$ (y)		$Pe = U_0 L/\kappa$	
			$\kappa = 100$ m^{2}s^{-1}	$\kappa = 2000$ m^{2}s^{-1}	$\kappa = 100$ m^{2}s^{-1}	$\kappa = 2000$ m^{2}s^{-1}
0.01	0.033	1.92	12.7	0.63	657.0	32.8
0.03	0.027	2.35	38.1	1.90	547.5	27.4
0.10	0.017	3.73	126.8	6.34	336.9	16.8

TABLE I: Flow parameters ε, U_0 and T for three different Stommel circulations calculated in a square basin with side-length $L = 2000$ km. Columns 4 to 7 show the Young time scales and the Péclet number for low and high diffusivity values.

Horizontal and vertical dispersion are studied separately. In Sec. III, we examine the horizontal dispersion of particles at the ocean surface for the following two-dimensional velocity fields:

1. Stommel flow and horizontal diffusion, $\boldsymbol{u_G} + \boldsymbol{u}_a$.

2. Stommel flow, Ekman drift and horizontal diffusion, $\boldsymbol{u_G} + \boldsymbol{u_D} + \boldsymbol{u}_a$.

3. Stommel flow, inertial effects and horizontal diffusion, $\boldsymbol{u_G} + \boldsymbol{u_I} + \boldsymbol{u}_a$.

4. Stommel flow, Ekman drift, inertial effects and horizontal diffusion, $\boldsymbol{u_G} + \boldsymbol{u_D} + \boldsymbol{u_I} + \boldsymbol{u}_a$.

In Sec. IV, the vertical dispersion analysis is performed by adding the three-dimensional Ekman velocity and starting the particles at a certain depth since the vertical velocity is zero at the surface. In these experiments, we do not consider inertial effects. Furthermore, the turbulent diffusivity is only horizontal. We study the two following cases:

1. Stommel flow and Ekman pumping, $\boldsymbol{u_G} + \boldsymbol{u_E}(|z| > d)$

2. Stommel flow, Ekman velocity and horizontal diffusion, $\boldsymbol{u_G} + \boldsymbol{u_E} + \boldsymbol{u}_a$.

III. HORIZONTAL DISPERSION

In this section, the horizontal particle dispersion on the ocean surface ($z = 0$) is analyzed when the primary advective mechanism is the Stommel circulation $\boldsymbol{u_G}$ plus diffusive effects $\boldsymbol{u_a}$. Our main interest is to examine the resulting dispersion when adding either the Ekman drift $\boldsymbol{u_D}$, inertial effects associated with $\boldsymbol{u_I}$, or both together. We consider a point charge of 3000 particles initially located at $(x_0, y_0) = (1/8, 1/4)$ (the southwest region of the flow domain). The results are similar when using different positions of the initial point charge.

A. Stommel circulation

In these experiments, the particles are advected by the Stommel flow and experience random fluctuations, so the advective velocity is $\boldsymbol{u_G} + \boldsymbol{u_a}$. This problem was neatly discussed by Young (1984) and Richards et al. (1995), who studied particle dispersion in western-intensified circulations. This subsection serves to illustrate the problem and as a way of validation.

Figure 2 shows the positions of the tracers at different times, as well as the trajectory of the center of mass, for $\varepsilon = 0.03$ and $Pe = 100$. Since $\varepsilon Pe = 3$, the problem is on the verge of the weak diffusive and intermediate regime (see Sec. II C 1). Initially ($t = 0.25T$), the particle cloud moves rapidly northward due to the intense boundary current in the west. The imposed diffusivity causes the cloud to disperse quickly. Then, at $t = 0.5T$, some particles begin a second cycle driven by the

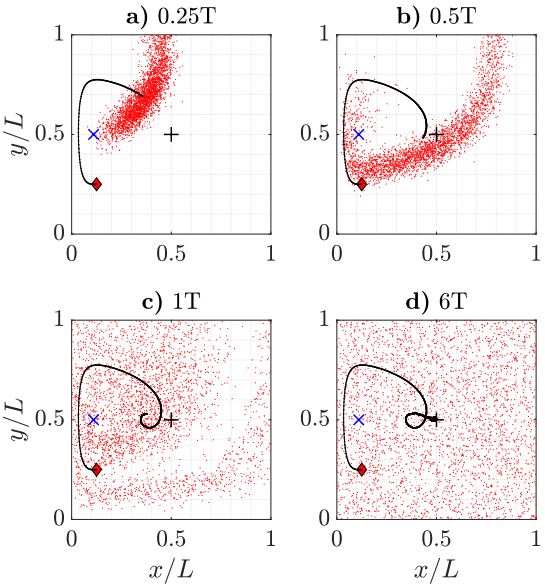

FIG. 2: Positions of 3000 particles (red dots) at different times in a Stommel flow with $\varepsilon = 0.03$ and a Péclet number $Pe = 100$, shown at the following times: (a) $0.25T$, (b) $0.5T$, (c) $1T$, and (d) $6T$. The particles were discharged at (1/8,1/4) (red diamond). The black curve represents the trajectory of the center of mass. The symbol $+$ indicates the basin's centre, and the blue symbol $\times$ represents the center of the Stommel gyre.

western boundary current, and others move more slowly in the northeastern part of the domain. At $t = T$, the particles are spread over most of the domain, and the center of mass begins to converge towards the basin's centre. At $t = 6T$, the tracers are distributed homogeneously throughout the basin, and the center of mass reaches the center of the domain. In this example, the Young time scale is about $T_\ell \approx 3T$. Experiments with different ε and Pe present similar results but at other times.

The particle dispersion is analysed in similar experiments with high and low diffusivity values. Figures 3a,b present the particle positions at the corresponding time scale T_ℓ. As expected, the particles already filled the domain at this time. The particle dispersion is analysed quantitatively by calculating the temporal evolution of the zonal (D_x^2) and meridional (D_y^2) relative dispersion components (see Sec. II B 2). Figures 3c,d show the dispersion curves for $Pe = 30$ and 550.

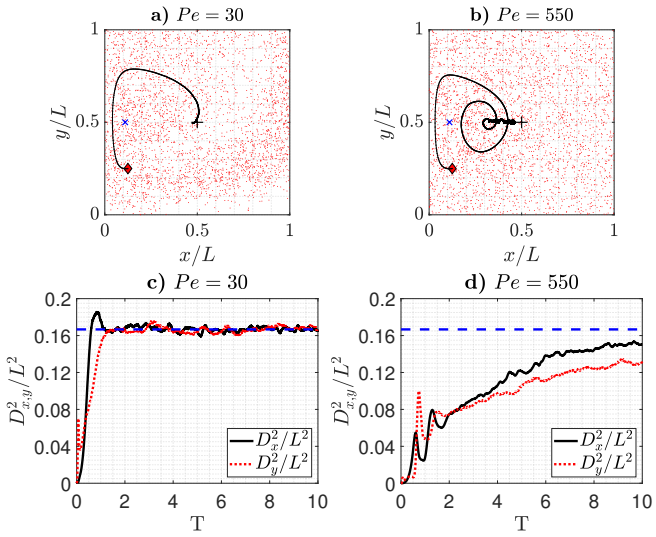

FIG. 3: (a)-(b): Positions of 3000 particles (red dots) at time T_ℓ in a Stommel flow with $\varepsilon = 0.03$ and different Péclet number: (a) $Pe = 30$ ($T_\ell/T = 0.9$), (b) $Pe = 550$ ($T_\ell/T = 16.5$). The black line is the trajectory of the center of mass. (c)-(d) Normalised relative dispersion components D_x^2/L^2 (black solid line) and D_y^2/L^2 (red dotted line) of cases (a) and (b), respectively. The blue dashed line is the dispersion limit per component, $1/6$.

The curves are normalized by the domain area L^2, so when the box is saturated, the curves reach the limit value 1/6. When using $Pe = 30$ (high diffusivity), the dispersion components quickly reach the maximum value in less than $2T$ (≈ 5 years), as seen in Figure 3a. The zonal dispersion grows faster than the meridional component and approaches the limit value first. Both components present small oscillations around 1/6 during the rest of the simulation. On the other hand, with $Pe = 550$ (low diffusivity, Figure 3b), the particles take longer to distribute in the basin and do not even reach the limit value after $10T$ (≈ 25 years).

The previous results can be summarized for a wide range of Pe by directly measuring a mixing time T_{mix} corresponding to the time the particles are spread over the whole basin. This procedure is equivalent to that followed by Richards et al. (1995), who estimated T_{mix} by solving the Eulerian advection-diffusion equation to track the distribution of a continuous tracer. In our Lagrangian experiments, such a time occurs when the relative dispersion reaches 90% of the limit

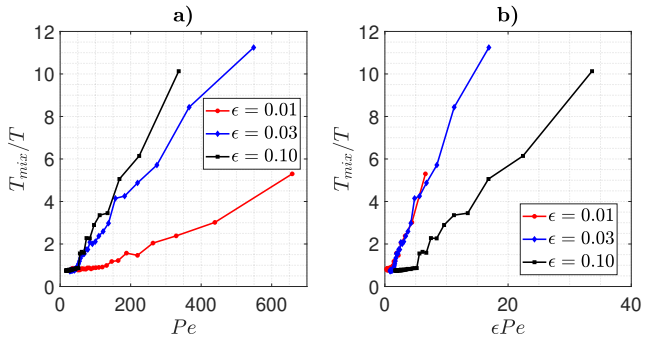

FIG. 4: (a) Normalised mixing time T_{mix}/T as a function of the Péclet number for three Stommel circulations. (b) T_{mix}/T against the Young time $T_\ell/T = \varepsilon Pe$ for the same Stommel flows. Note the collapse of the curves for $\varepsilon = 0.01$ and 0.03.

value ($D^2_{max}/L^2 = 1/3$). The mixing times normalized with the corresponding T for each Stommel flow, T_{mix}/T, are shown in Figure 4a. Of course, the lower the diffusivity, the longer the mixing time. In general, our calculations using this criterion coincide with those presented by Richards et al. (1995) (see their figure 8). On the other hand, it is expected that T_{mix} is of the order of the Young scale T_ℓ, as mentioned in section II B 2. From its definition (34), note that $T_\ell = \varepsilon PeT$. In Figure 4b, we plot T_{mix}/T against $T_\ell/T \equiv \varepsilon Pe$. The curves for $\varepsilon = 0.01$ and 0.03 collapse in a linear relationship $T_{mix} \sim (4/5)T_\ell$. For $\varepsilon = 0.1$, the linear relationship is less clear and has a smaller slope, $T_{mix} \sim (2/7)T_\ell$. For the present dispersion regimes and Stommel circulations, it is safe to consider T_ℓ as a time scale at which the tracers are already dispersed over the whole domain.

The analyses of this section have shown the general behavior of the tracers in Stommel circulations: the particles tend to fill the domain after a specific time, and the center of mass converges to the center of the domain. These introductory results will allow us to appreciate the profound differences caused by the Ekman drift and inertial effects.

B. Stommel flow and Ekman drift

In this section, the advective velocity includes the Ekman drift, so the total velocity is $\boldsymbol{u_G} + \boldsymbol{u_D} + \boldsymbol{u_a}$. Figure 5a,b shows the position of the particles at the corresponding scale T_ℓ using a Stommel flow with $\varepsilon = 0.03$, and high and low diffusivity values ($Pe = 30$ and 550, respectively,

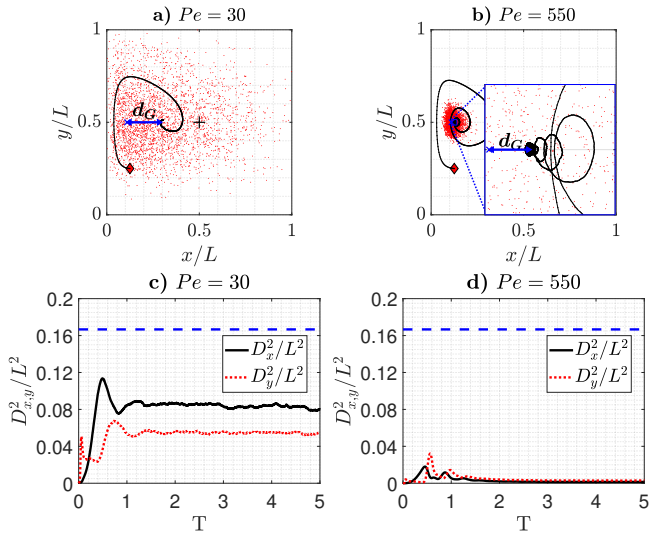

FIG. 5: (a)-(b) Particle positions at time T_ℓ and (c)-(d) time evolution of the relative dispersion components as in Figure 3, but now for experiments including Ekman drift. The inset in (b) shows the zoom of a square area near the gyre centre. The zonal blue line in (c)-(d) is the distance d_G between the center of the gyre and the actual position of the center of mass.

see Figure 4). It is found that using a small Péclet number $Pe = 30$ (high diffusivity), the particles end up dispersed but without covering the entire domain (Figure 5a). In fact, the distribution is skewed to the northwest, while the southern region is almost empty. In addition, the trajectory of the center of mass (black curve) indicates that the particles end up, on average, at a fixed position located at a zonal distance d_G from the gyre center. For larger Pe (low diffusivity), the tracers rotate around the basin and accumulate in a small region near the centre of the gyre (Figure 5b). In this case, the centre of mass converges rapidly towards a point located at a much smaller distance d_G (in comparison with the previous case), as shown by the zoom in the inset. Thus, with low diffusivity, the distance d_G decreases; that is, the center of mass approaches the center of the Stommel circulation. In the absence of diffusion, the Ekman drift causes d_G to be zero.

The most important result is that the tracers do not fill the domain at time T_ℓ, as they would in the absence of the Ekman drift. Also, the tracers do not spread out over the domain for later times. Furthermore, the particles reach a quasi-stable distribution that remains during the whole

simulations. This behaviour can be measured with the relative dispersion. Figures 5c,d show the time evolution of the relative dispersion components, D_x^2 and D_y^2, in the experiments discussed before. Note that the plots in both panels have the same scale; thus, we can compare the substantial differences resulting from high and low diffusivity values. For both cases, the dispersion components have a very intense increase at the beginning ($t < 1.5T$), reflecting the moment the tracers pass for the first time in the boundary layer to the west. For $Pe = 30$ (Figure 5c), we confirm that the zonal dispersion is greater than the meridional dispersion (as observed before from the particle distribution in Figure 5a) because the Ekman drift converges towards the mid-latitude of the basin. The quasi-regular behaviour of the dispersion curves corroborates that the average particle distribution does not change at long times. For $Pe = 550$, a much smaller dispersion is achieved at the beginning, as shown in Figure 5d (e.g. at $t = 0.5T$). Afterwards, the tracers rapidly converge into a small region near the gyre centre, decreasing the dispersion (see also the particle distribution in Figure 5b). A stable dispersion is reached for longer times that fluctuates around a small value.

The quasi-stable state can also be observed in the time evolution of the total dispersion D^2 and of distance d_G. It will be convenient to calculate the equilibrium values of these two numbers. The procedure consists of performing long enough simulations (typically between 7 and $10T$) to appreciate from the respective time series that the equilibrium state has been reached. The equilibrium value corresponds to the average of the last $3T$ periods of the simulation. We performed several experiments for a wide range of Péclet numbers to generalise the results.

Figures 6a,b show the equilibrium values of the total relative dispersion, D_{eq}^2, and distance d_G as a function of εPe for three different Stommel flows. The curves in panel (a) indicate to what extent the particles are dispersed over the whole domain. Remarkably, the curves collapse for any εPe. Since all the curves are below the maximum value (1/3), it is concluded that the Ekman drift prevents total mixing in all cases, in contrast with the purely Stommel flow. The experiments with higher dispersion are found for smaller Pe. On the other hand, distance d_G in panel (b) is an indirect measure of the particle concentration near the gyre centre. The curves for d_G behave similarly to those for D_{eq}^2: the curves collapse, indicating that in all cases the particles are more separated from the gyre center for smaller Pe.

How long does it take to reach the equilibrium state? We will call T_{eq} the time to reach the quasi-steady particle distribution in the Stommel-Ekman system. This time can be directly measured in experiments with different Péclet numbers and different Stommel flows. The criterion based on the equilibrium value D_{eq}^2 consists of calculating the corresponding standard deviation σ (within

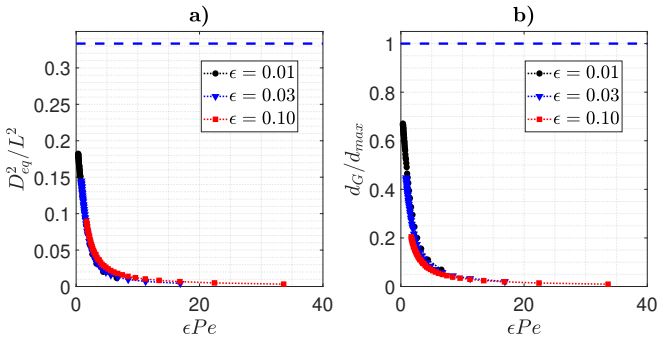

FIG. 6: (a) Normalised equilibrium relative dispersion D^2_{eq}/L^2 as a function of εPe for Stommel circulations with $\varepsilon = 0.01$, 0.03, 0.10 and Ekman drift. The maximum dispersion is $1/3$ (upper dashed line). (b) Same as (a) for the normalised equilibrium distance d_G/d_{max}. The maximum value d_{max} is the distance between the gyre's centre and the basin's centre (see text).

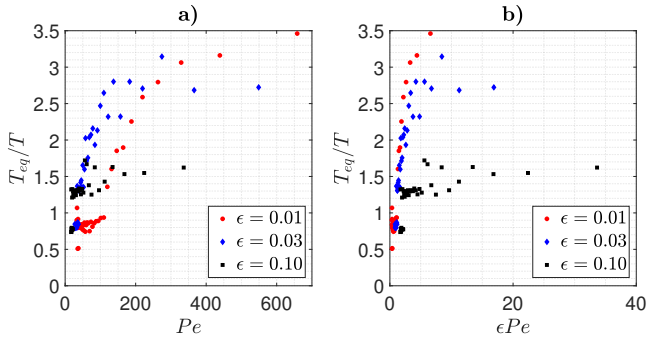

FIG. 7: (a) Normalised equilibrium time T_{eq}/T as a function of the Péclet number for three Stommel circulations and Ekman drift. (b) T_{eq}/T against the Young time $T_\ell/T = \varepsilon Pe$ for the same Stommel flows. Note the collapse of the curves for $\varepsilon = 0.01$ and 0.03.

the same time frame) and then finding the time at which the dispersion enters within the interval $D^2_{eq} \pm 4\sigma$ and remains there (which was verified directly from the time series). Figure 7 presents the period T_{eq}/T against Pe in an analogous way as the mixing time was plotted in Figure 4. In this case, the results are much noisier. Nevertheless, T_{eq}/T is approximately one for low Pe. For larger Pe (lower diffusivity), it becomes approximately constant: $T_{eq}/T \approx 3$ to 3.5 for $\varepsilon = 0.01$ and 0.03, and $T_{eq}/T \approx 1.5$ for $\varepsilon = 0.1$. To compare with the Young scale, Figure 4b shows T_{eq}/T

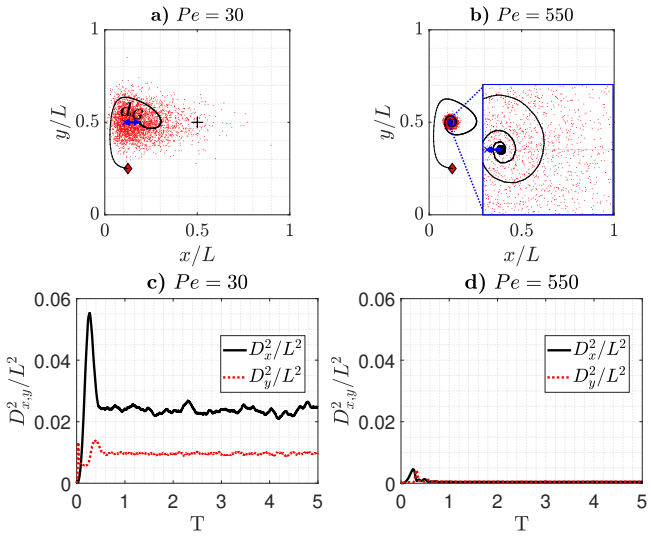

FIG. 8: (a)-(b) Particle positions at time T_ℓ and (c)-(d) time evolution of the relative dispersion components as in Figures 3 and 5, but now for experiments with inertial particles. The inset in (b) shows the zoom of a square area near the gyre centre. The zonal blue line in (c)-(d) is the distance d_G between the center of the gyre and the actual position of the center of mass.

against $T_\ell/T = \varepsilon Pe$. As found for the purely Stommel flow, the results collapse for low εPe values (especially for the circulations with $\varepsilon = 0.01$ and 0.03).

C. Inertial particles in Stommel flows

Now we examine the horizontal dispersion with inertial particles and no Ekman drift. The total velocity is $\boldsymbol{u_G} + \boldsymbol{u_I} + \boldsymbol{u_a}$. Inertial effects are included by associating a size and weight to the particles, so two variables can modify the trajectories: the radius of the particles r and their buoyancy δ. Recall that $\delta = 1$ means a completely sunken sphere; $\delta = 2$ represents buoyancy where only half protrudes from the surface; and $\delta = 6.4$ three-quarters of the sphere emerges from the surface. In all the experiments in this section, the Stommel circulation has $\varepsilon = 0.03$.

Consider a point charge of particles with $r = 0.1$ m and $\delta = 2$ initially located at the same position as in previous experiments. Figures 8a,b show the particle positions at T_ℓ for the high ($Pe = 30$) and low ($Pe = 550$) diffusivity values (compare with Figures 3 and 5). For the case

of high diffusivity, the tracers are distributed in a region around the center of the gyre (Figure 8a). When comparing with the dispersion found for the Stommel flow with constant Ekman drift (Figure 5a), it is observed that the inertial effects are more effective in concentrating particles. Indeed, the cloud is less dispersed in the inertial case. Furthermore, the distance d_G is smaller with inertial particles. The agglomeration is attributed to the effect of wind drag on the inertial particles due to their radius and buoyancy, which generate a negative divergence more significant than that of the Ekman drift. For low diffusivity (Figure 8b), the particle cloud concentrates quickly near the gyre's centre, and there is still a zonal distance d_G, as the zoom shows.

To compare the effect of modifying the particle characteristics (radius and buoyancy), Figure 9 shows the positions of inertial particles with different r and δ in simulations with an intermediate diffusivity ($Pe = 100$). The Young time is $T_\ell \approx 3T$. Figures 9a,b present the results with particles with different radii but having the same buoyancy. For small particles (Figure 9a), the distribution is zonally elongated but limited in the meridional direction between $0.2 \lesssim y \lesssim 0.8$. Furthermore, the center of mass ends up very close to the basin's centre. When considering bigger tracers with the same buoyancy (Figure 9b), they agglomerate very quickly in the gyre's centre. These behaviours and the enormous difference between them when modifying r are associated with the Stokes drag, which depends directly on the particle size.

To explain the previous argument, let us analyze the equation for the inertial velocity defined in (21). The first two terms represent the motion influenced by the ocean, $(1-\alpha)\boldsymbol{u_O}$, and the wind drag $\alpha\boldsymbol{u_A}$, which are non-divergent flows as defined in the Stommel model. On the other hand, the last term provides a negative divergence regulated by the parameters α, R, and τ. Changing the particle size modifies only the Stokes time τ, while α and R remain constant (see Appendix). Therefore, small particles have short response times to the current displacing them, and hence, they follow the flow $(1-\alpha)\boldsymbol{u_O} + \alpha\boldsymbol{u_A}$. Conversely, large particles have long reaction times, causing them to continue their motion while deviating intensely to the right due to Coriolis.

On the other hand, Figures 9c,d compare experiments with particles having different buoyancy but the same radius. For the case with smaller buoyancy, the final distribution is wider ($\delta = 1.05$, Figure 9c) than for tracers with the same radius but greater buoyancy ($\delta = 4$, Figure 9d). To explain the distribution with a different δ, note that $\delta \to 1$ implies that the particle tends to be submerged, so its movement would be dominated by the geostrophic current (defined by the Stommel circulation) and the fluid drag associated with its finite size. The resulting particle distribution is similar to that observed with Ekman drift (compare Figure 9c with Figure 5a), but

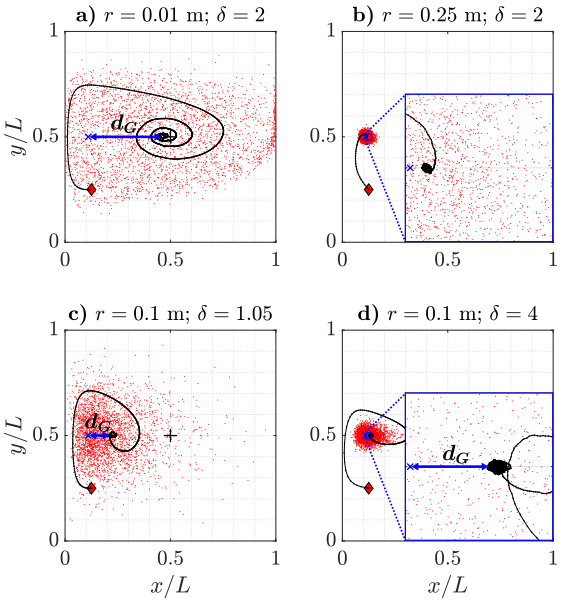

FIG. 9: Particle positions at time T_ℓ in experiments with a Stommel flow $\varepsilon = 0.03$, Péclet number $Pe = 100$, and inertial particles with: (a) $r = 0.01$, $\delta = 2.0$; (b) $r = 0.25$, $\delta = 2.0$; (c) $r = 0.1$, $\delta = 1.05$; (d) $r = 0.1$, $\delta = 6.4$. Symbols and curves as in Figure 5. The insets in (b) and (d) show a zoom of a square area near the gyre centers.

the physical mechanism is very different. On the contrary, the more the tracers float ($\delta > 1$), the more the wind drags them. Furthermore, the convergence of the centre of mass towards the centre of the gyre increases (Figure 9d). Contrary to the effect of changing particle size, buoyancy alters all parameters (α, R, and τ), with the most significant being the wind drag, which increases the velocity of the particles.

The particle distributions, when including inertial effects, reach an equilibrium state that remains during the whole simulations, as we found in the Ekman drift experiments. Similarly, such states can be identified with the quasi-steady values attained by the total relative dispersion, D^2_{eq}, and distance d_G. Thus, we ran several experiments for different Péclet numbers to make general statements. Figures 10a,c show the quasi-steady relative dispersion as a function of Pe for different values of r and δ. We find the same behaviour for any radius and buoyancy: D^2_{eq} decreases with larger Pe (i.e., with lower diffusivity). For example, for a constant buoyancy $\delta = 2$ (Figure 10a),

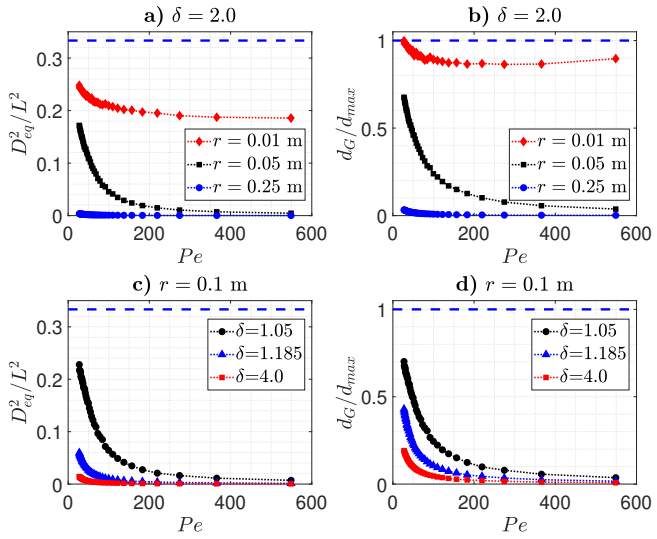

FIG. 10: (a)-(c) Equilibrium relative dispersion D_{eq}^2/L^2 as a function of Pe for a Stommel circulation with $\varepsilon = 0.03$ and using inertial particles. (a) Constant buoyancy $\delta = 2$ and radii $r = 0.01$, 0.05 and 0.25 m. (b) Constant radius $r = 0.1$ m and buoyancy values $\delta = 1.05$, 1.185 and 4. (b)-(d) Same as (a)-(c) for distance d_G normalised with d_{max}.

smaller particles are more dispersed over the basin (see e.g. the black curve for $r = 0.01$ m). The reason is that bigger particles have more inertia, so they converge more and disperse less. At a constant radius (Figure 10c), the major dispersion is found for nearly submerged particles (black curve for $\delta = 1.05$). Emerged particles tend to concentrate more because they are prone to being dragged by the wind. Figures 10b,d present the results for d_G, which behaves in a similar way as D_{eq}^2. Recall that smaller d_G/d_{max} values mean that the centre of mass converges more towards the gyre's centre.

D. Inertial particles in Stommel flows with Ekman drift

Finally, we consider inertial particles advected by the Stommel flow and the Ekman drift. The total velocity is $\boldsymbol{u_G} + \boldsymbol{u_D} + \boldsymbol{u_I} + \boldsymbol{u_a}$. As shown in the previous sections, the Ekman drift and inertial effects significantly modify the particle dispersion (in comparison with the purely Stommel advection) by bringing the center of mass closer to the center of the gyre. Now, we are interested

in combining both effects by varying the size and buoyancy of the tracers in the presence of Ekman drift.

When repeating the same analyses done in previous subsections, it is found that, qualitatively, the particle distributions at time T_ℓ are very similar to those found in the experiments with inertial particles and no Ekman drift (e.g. those in Figure 9). Once again, it is found that the particle distributions tend towards a stable configuration at long times at which the dispersion reaches an equilibrium value. Figure 11 shows the quasi-steady relative dispersion as a function of Péclet for different radii r and buoyancy δ. The resulting curves have the same trend observed in cases without Ekman drift, shown in Figure 10. The important difference is that inertial and Ekman effects reinforce particle convergence; therefore, the equilibrium dispersion reaches smaller values. Also, distance d_G becomes smaller; that is, the tracers concentrate more.

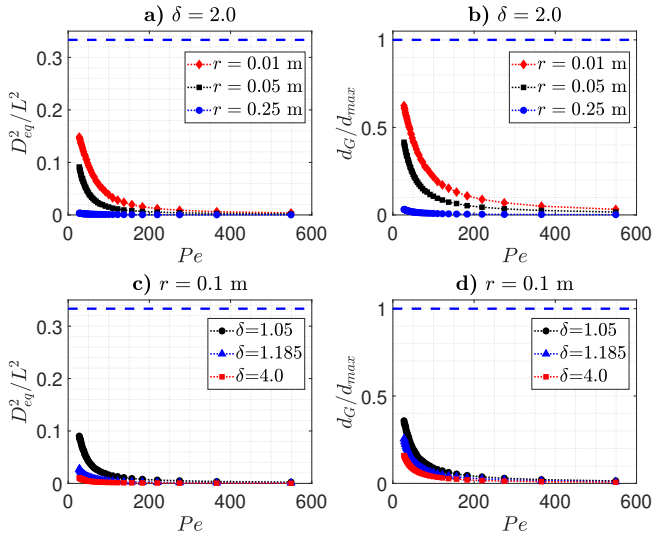

FIG. 11: Same as in Figure 10 but now adding the Ekman drift to the inertial particles. (a)-(c) Equilibrium relative dispersion D^2_{eq}/L^2, and (b)-(d) distance d_G normalised with d_{max}.

IV. VERTICAL DISPERSION

This section studies three-dimensional flows by including the Ekman vertical velocity w_E, defined in (18). For the negative-curl Stommel wind, the vertical motions generated in the surface

boundary layer sink the tracers. We aim to investigate the vertical distribution of particles as they are advected horizontally. The thickness of the Ekman layer is assumed $d = 50$ m. Once again, we consider the Stommel flow with $\varepsilon = 0.03$. No inertial effects were considered.

A. Stommel flow with Ekman pumping

To illustrate the displacement of particles due to the vertical Ekman pumping in the Stommel circulation, we performed a simulation with a large number of tracers distributed uniformly over a horizontal plane at $z = -2d$ (below the Ekman layer). For this case, turbulent diffusion is omitted ($Pe = \infty$). The three-dimensional advection velocity is $\boldsymbol{u_G} + \boldsymbol{u_E}$, where now $\boldsymbol{u_G} = (u_G, v_G, 0)$. In this region, the horizontal components of the Ekman velocity u_E, v_E (16)-(17) are very small and only the Ekman pumping w_E (19) remains, such that $\boldsymbol{u_E} \approx (0, 0, w_E)$. Of course, $w_E < 0$ because it is caused by the Stommel wind with a negative curl. In this experiment, $|w_E|_{max} = 1.6 \times 10^{-6}$ ms$^{-1} \approx 0.14$ m/day.

Figure 12 shows the three-dimensional particle positions and the trajectory of the centre of mass at time $2.5T$ from three perspectives: from $y = 0$ ($x - z$ plane, left panel), $x = L$ ($y - z$ plane, middle panel) and $z = 0$ ($x - y$ plane or top view, right panel). The colour of the particles indicates the depth at which they are found. The particles near the gyre's centre on the western side have reached a higher depth. The reason for this distribution is because the particles that are initially near the gyre centre circulate all the time in closed streamlines where they experience a more intense vertical velocity and, therefore, sink further in that region. In contrast, particles found in other streamlines spend much of their transit time at the northern and southern parts of the basin, where the vertical velocity is weak, and therefore, they sink less. Particles that started near the corners go down a few meters.

The lateral views in Figure 12 show that the centre of mass remains almost at the centre of the basin as the tracers circulate and, at the same time, sink. The center of mass descended approximately 300 m, while the particles near the gyre center reached up to 400 m. Another characteristic is the "layering" observed in the vertical planes, especially in the (x, z) plane. This effect is a manifestation of the downward spiralling trajectories associated with the horizontal distribution of the vertical velocity w_E.

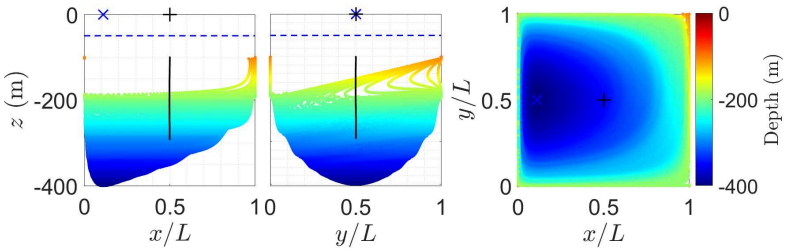

FIG. 12: Lateral and top view perspectives of the three-dimensional positions of 160,000 particles at $t = 2.5T$ (≈ 5.8 years) in a Stommel flow ($\varepsilon = 0.03$) with Ekman pumping. The tracers were uniformly distributed in a horizontal plane $z = -2d$ below the Ekman layer. The solid black line is the downward trajectory of the centre of mass. The horizontal dashed line indicates the Ekman layer at $z = -d$. Symbols represent the basin centre ($+$) and the gyre centre ($\times$). In this experiment, there is no diffusion.

B. Stommel-Ekman flow with diffusion

Now, we study the dispersion of a point charge (3000 particles) released within the surface boundary layer in the Stommel flow; thus, the three velocity components of the Ekman velocity are initially different from zero. A constant horizontal turbulent diffusivity is also added, so the full velocity is $\boldsymbol{u_G} + \boldsymbol{u_E} + \boldsymbol{u_a}$. The Stommel and Ekman flows are the same as in the previous section ($\varepsilon = 0.03$ and $d = 50$ m). The initial horizontal position of the point charge is the same used in all cases studied in Sec. III. The initial depth is almost at the surface, $z_0 = -10^{-2}$ m (the tracers cannot begin exactly at $z = 0$ because w_E is zero there). Since the initial vertical position is so close to the surface, the particles will mainly experience the Ekman drift due to the horizontal components u_E, v_E while slowly sinking in spiral trajectories until they leave the Ekman layer and continue sinking due to the Ekman pumping. This experiment aims to analyze the horizontal and vertical distribution of the tracers while they are sunk, as well as the effects of considering different diffusivity values.

Figure 13 presents the lateral perspectives and top view of the particle positions for different Péclet numbers after $6.4T$ (≈ 15 years; in this case $T = 2.35$ years, see Table I). The trajectory of the center of mass is also shown. These distributions indicate several relevant results.

(i) For high diffusivity ($Pe = 30$, panels in Figure 13a), the particles redistribute at the surface

while slowly sinking. After leaving the Ekman layer, they continue downward towards $|z| > d$ at the Ekman pumping speed. At these depths, the Ekman convergence towards the gyre centre disappears, and, therefore, the diffusive effects in the Stommel circulation dominate the horizontal motion and distribute the tracers over the entire domain, as shown from the top view at the right panel. The center of mass indicates that the average depth is about 250 m, and there is a high dispersion in the vertical direction. The x-side view (left panel) shows more significant subsidence to the west of the domain. (ii) For the intermediate diffusivity ($Pe = 100$, panels in Figure 13b), similar processes are observed, but in this case, the tracers sink more on average (more than 300 m). The skewed distribution towards the western wall is more evident than in the previous example (left panel). (iii) At low diffusivity ($Pe = 550$, panels in Figure 13c) the tracers agglomerate around the gyre centre while being on the surface. Then, they descend almost together until reaching depths of about 380 m. On average, the tracers sink more than in previous cases. The reason is that the convergence associated with the Ekman flow within the boundary layer ($|z| < d$) keeps the tracers close to the gyre's centre, where the sinking is intensified. The final horizontal dispersion (right panel) shows that the particles have not filled the domain yet, but they will eventually fill it because there are no converging effects at those depths.

To quantify the descent of the tracers, the square root of the absolute vertical dispersion $\sqrt{A_z^2}$ is calculated. Recall from definition (31) that this quantity is the standard deviation of the vertical positions measured from the initial depth z_0. Figure 14a shows $\sqrt{A_z^2}$ as a function of time for different Pe numbers. The tracers slowly descend through the Ekman layer during the first four T periods (≈ 9 years). Once they leave the Ekman layer, the vertical velocity reaches a constant value (~ 0.14 m/d), so a linear increase is observed for any diffusivity. The particles sink deeper for lower diffusivity because the cluster remains more agglomerated near the gyre's centre (red curve). The depths reached for high, intermediate and low diffusivity are 236, 301 and 355 m, respectively. The square root of the relative vertical dispersion $\sqrt{D_z^2}$ is also calculated and plotted in Figure 14b. This quantity measures the cloud dispersion in the z-direction, which can also be appreciated in the side views in Figure 13. The $\sqrt{D_z^2}$ curves show high values for $Pe = 30$ and 100, while the low diffusivity experiments ($Pe = 550$) present an almost null dispersion because most of the tracers descend together.

Figure 15 shows the normalized horizontal dispersion for the cases considered before to measure the effect of turbulent diffusivity in the horizontal dispersion as the tracers sink. For the lower and intermediate Pe number, the dispersion curves (black and blue) grow and reach a plateau be-

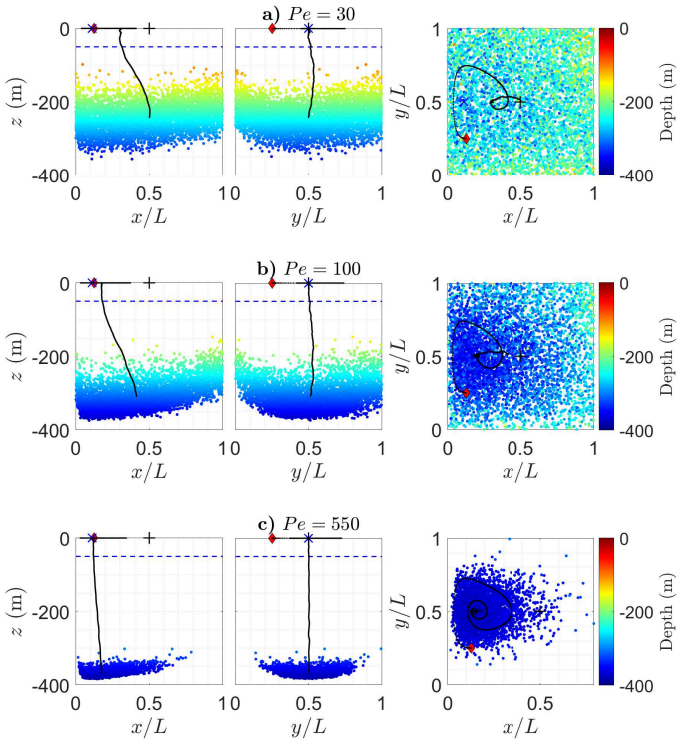

FIG. 13: Lateral and top view perspectives of 5000 particles in point charge experiments at time $6.4T$ in a Stommel flow ($\varepsilon = 0.03$, $T = 2.35$ years) with the three-dimensional Ekman velocity and different Péclet numbers: (a) $Pe = 30$, (b) $Pe = 100$, (c) $Pe = 550$. The particles start at $(x_0, y_0) = (1/4, 1/8)$ (red diamond) and almost at the surface (see text). Symbols, lines, and colours as in Figure 12.

tween T and $4T$ (3 and 9 years, respectively), indicating the saturation observed in the Stommel flow with Ekman drift (see Figure 5a). Up to this time, the particles slowly sink but are still within the boundary layer, and therefore, they are affected by the surface Ekman drag. After $4T$, the tracers leave the Ekman layer, so the convergence generated by the surface drag disappears. Consequently, the Stommel advection redistributes the tracers over the whole basin: for high diffusivity $Pe = 30$, the horizontal dispersion increases rapidly until reaching the saturation value of 1/3 at the end of the simulation. Thus, the greater the diffusivity, the less time it takes for the trac-

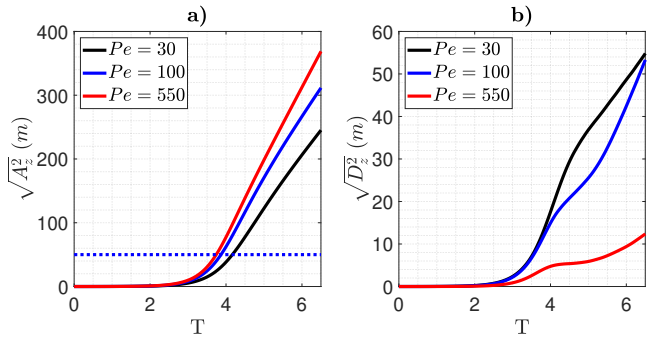

FIG. 14: (a) Time evolution of the square root of the absolute vertical dispersion $\sqrt{A_z^2}$ for the experiments shown in Figure 13. The horizontal dashed line indicates the Ekman layer thickness $d = 50$ m. (b) Same as (a) but for the vertical relative dispersion $\sqrt{D_z^2}$.

ers to distribute homogeneously throughout the domain until the maximum horizontal dispersion is reached. The particles present much less dispersion for the lowest diffusivity ($Pe = 550$, red curve) and do not fill the basin yet.

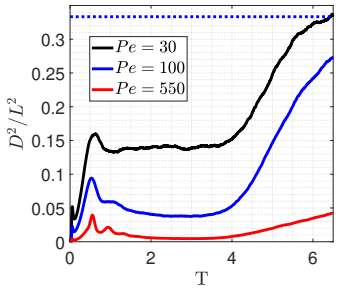

FIG. 15: Normalized horizontal relative dispersion D^2/L^2 for the experiments shown in Figure 14. The blue dashed line is the limit of the horizontal dispersion, 1/3.

V. DISCUSSION AND CONCLUSIONS

We studied horizontal and vertical Lagrangian dispersion in single-gyre Stommel flows with Ekman and inertial effects, and including diffusion with a stochastic model. Horizontal dispersion was examined in Sec. III, where we demonstrated differences in the particle distributions when

considering the surface Ekman drift and inertial effects as a function of horizontal diffusion measured with the Péclet number *Pe*. In Sec. IV, we considered the three-dimensional problem by adding the full Ekman velocity to the Stommel flow (without inertial effects).

The main results on horizontal dispersion are the following:

- It was already known that the Stommel flow alone is efficient to mix a tracer over the whole basin in a time scale T_{mix} that depends on ε, *Pe*, and the circulation time T (Richards et al., 1995). Here, we found that such a dependence can be condensed in a proportional relationship with the time scale $T_\ell = \varepsilon L^2/\kappa$ proposed by Young (1984); that is $T_{mix} \approx aT_\ell \equiv a\varepsilon PeT$ with a a dimensionless constant. For small ε (between 0.01 and 0.03), $a \approx 4/5$; for greater ε, constant a is smaller (see Figure 4).

- When including Ekman drift, we confirm (not surprisingly) that diffusive effects are surpassed, so the particles aggregate within a limited region (see, e.g. Kubota, 1994; Maximenko et al., 2012). The experiments showed that the surface drift generates convergence that constantly accumulates tracers towards the gyre's centre until reaching a quasi-equilibrium without filling the domain. The equilibrium state is measurable: it consists of a particle distribution with quasi-steady values of (i) the total relative dispersion (measuring the cloud dispersion) and (ii) the zonal distance d_G between the center of the gyre and the particles' center of mass. These characteristics are summarised in Figure 6 for different *Pe* and ε. Furthermore, the process to reach the equilibrium occurs in a time scale T_{eq} that is shorter, in general, than T_{mix}. More precisely, it is found that T_{eq} is of the same order as T_ℓ (Figure 7).

- In the presence of inertial effects, characterized by particle size and buoyancy, the tracers accumulate around the gyre centre by different mechanisms from the Ekman drift. Large particles tend to follow the inertial motion imprinted by the ocean current and the Stommel wind, causing a deviation to the right of these fields. Therefore, this motion generates convergence towards the gyre centre. On the other hand, a light tracer floats more, allowing the wind to exert a more significant drag on it, which translates into a greater Coriolis force, deflecting the tracer to the right of its motion. As in the Ekman drift case, the cloud of particles reaches a quasi-steady state without filling the domain in a time scale shorter than T_{mix}. When comparing the Ekman drift and inertial effects (see Figures 5 and 8), we conclude that the latter is more efficient for concentrating particles near the gyre centre, though the de-

tailed difference depends on the specific particle size and buoyancy. These results point out that the traditional explanation of garbage patches in subtropical gyres based on the linear Ekman dynamics (van Sebille et al., 2012; Maximenko et al., 2012) might be insufficient when ignoring inertial effects (Beron-Vera et al., 2016).

To study vertical dispersion, we added the full Ekman velocity to the Stommel circulation and ignored inertial effects. Given the negative curl of the Stommel wind, the vertical velocity is negative, so the particles sink. The following aspects are highlighted:

- With or without horizontal diffusion, and using initial positions below the Ekman layer or at the surface, the particles sink at a greater depth around the centre of the gyre at the basin's western side (as shown in Figures 12 and 13). This uneven distribution is formed because, around that point, the Stommel streamlines keep the particles in a region where the vertical velocity is most significant. The deeper (shallower) positions of the tracers at the west (east) coincide with the climatological shape of the thermocline in large-scale basins (Luyten et al., 1983).

- A relevant result is the horizontal dispersion generated as the particles sink. When the particles start very close to the surface in experiments with horizontal diffusion, they are subject to the Ekman drift while slowly sinking. As a result, the particles gather around the gyre's centre because of the horizontal Ekman drift, as described for the purely horizontal dispersion problem. However, once the particles sink beyond the Ekman layer, the surface effects disappear, and only the horizontal Stommel flow remains, together with the vertical Ekman pumping. Consequently, the particles disperse horizontally (while sinking) throughout the whole domain (see the dispersion curves in Figure 15). The implications are considerable because the surface tracers agglomerated at the surface spread over the whole domain when sinking below the Ekman layer. Although this effect would be reduced by the slower motions of the deep ocean, it seems a plausible mechanism suggesting a wide spread of sinking tracers. The deep horizontal dispersion might promote or enhance the exchange of matter between different regions. This mechanism has been suggested in global-scale subsurface transport simulations of passive microplastic between subtropical and subpolar gyres, potentially contributing to the pollution of polar areas (Wichmann et al., 2019).

For future research, inertial effects on sinking particles should be considered. To achieve this, the standard Maxey–Riley equation in three dimensions, including the Coriolis force, should be

used. Assuming that finite-size particles sink due to gravity sufficiently slowly, representing heavy particles, and ignoring Ekman transport, the results of Beron-Vera et al. (2015) and Beron-Vera (2021) suggest a concentration in the gyre interior. Thus, it would be of interest to evaluate the competition between this convergence and the opposite effect due to the horizontal dispersion observed here.

The models used here are ideal and limited. They do not fully represent the mechanisms present in the ocean and ignore many others. However, their simplicity allows for a better understanding of the behaviour of the tracers and the results and, therefore, provides a primary but well-founded estimate of the horizontal and vertical dispersion in meso- and large-scale systems. Using similar models might help improve our understanding of more complex phenomena. Part of our current research efforts point in that direction.

ACKNOWLEDGMENTS

J.R.B.V. gratefully acknowledges the financial support given by the Departmento de Oceanografía Física, CICESE, and for the scholarship from Consejo Nacional de Humanidades, Ciencias y Tecnologías, CONAHCYT, México (CVU 1131888). F.J.B.V.'s work has been supported by the National Science Foundation under grant number OCE2148499.

Appendix: Inertial particles

This Appendix explains some of the geometric factors of the inertial model of Beron-Vera et al. (2019), subsequently simplified in Olascoaga et al. (2020) and Beron-Vera (2021). The parameters α, R and τ in (21) are defined from the radius r and buoyancy δ of the particle as

$$\alpha = \frac{\gamma\Psi}{(1-\Psi)+\gamma\Psi}, \qquad \gamma = \frac{\mu_A}{\mu_O}, \tag{A.1}$$

$$\tau_s = \frac{1-\frac{1}{6}\Phi}{((1-\Psi)+\gamma\Psi)\delta} \cdot \frac{r^2}{3\mu_O/\rho_O}, \tag{A.2}$$

$$R = \frac{1-\frac{1}{2}\Phi}{1-\frac{1}{6}\Phi}, \tag{A.3}$$

where the constant Ψ is proportional to the area projected in the direction of the flow (A_A), and Φ depends on the height of the particle above the sea level (h_A).

Constants Ψ and Φ defined in terms of δ are

$$\Psi(\delta) = \frac{A_A}{\pi r^2} = \frac{1}{\pi}\cos(1-\Phi) - \frac{(1-\Phi)\sqrt{1-(1-\Phi)^2}}{\pi}, \tag{A.4}$$

$$\Phi(\delta) = \frac{h_A}{r} = \frac{i\sqrt{3}}{2}\left(\frac{1}{\varphi} - \varphi\right) - \frac{1}{2\varphi} - \frac{\varphi}{2} + 1, \tag{A.5}$$

with

$$\varphi(\delta) := \sqrt[3]{i\sqrt{1-(2\delta^{-1}-1)^2} + 2\delta^{-1} - 1}. \tag{A.6}$$

The height and area submerged in water can be easily obtained from their superior complements, that is

$$h_O = (2-\Phi)r, \tag{A.7}$$

$$A_O = \pi(1-\Psi)r^2. \tag{A.8}$$

To better understand the dependence of the parameters on the radius and buoyancy of the particle, Table II shows the values taken by the constants Ψ, Φ, α, R and τ when the sphere is completely submerged ($\delta = 1$) and when its radius is minimal ($r \to 0$). It should be noted that only τ has dimensions (Stokes time), and the parameter α provides the intensity of the drag due to the oceanic geostrophic current ($\boldsymbol{u_O}$) and the wind ($\boldsymbol{u_A}$). It is important to emphasize that the upper δ limit is not infinity. When the particle's density approaches that of air, the principle of Archimedes should be used to calculate the submerged volume of the particle, not as an approximation of δ (see Olascoaga et al., 2020).

Parameter	$\delta = 1$	$r \to 0$
Φ	0	$\sim$
Ψ	0	$\sim$
α	0	$\sim$
τ_s	$\frac{r^2}{3\mu_O/\rho_O}$	0
R	1	$\sim$

TABLE II: First column: parameters in the inertial model that determine the influence of the wind and water on a spherical particle with radius r and buoyancy δ in the air-water interface. Columns 2-3: value of the parameters for the lower and upper δ-limits and small particles. Symbol $\sim$ in last column indicates r-independence.

REFERENCES

Amador González, M. F., Zavala Sansón, L., 2023. Surface dispersion of coastal discharges in north america towards the great pacific garbage patch. Marine Pollution Bulletin 191, 114961.

Berloff, P. S., McWilliams, J. C., 2002. Material transport in oceanic gyres. part ii: Hierarchy of stochastic models. Journal of Physical Oceanography 32 (3), 797–830.

Berloff, P. S., McWilliams, J. C., Bracco, A., 2002. Material transport in oceanic gyres. Part I: Phenomenology. Journal of Physical Oceanography 32 (3), 764–796.

Beron-Vera, F., 2021. Nonlinear dynamics of inertial particles in the ocean: From drifters and floats to marine debris and sargassum. Nonlinear dynamics 103 (1), 1–26.

Beron-Vera, F., Olascoaga, M., Haller, G., Farazmand, M., Triñanes, J., Wang, Y., 2015. Dissipative inertial transport patterns near coherent lagrangian eddies in the ocean. Chaos 25, 087412.

Beron-Vera, F. J., Olascoaga, M. J., Lumpkin, R., 2016. Inertia-induced accumulation of flotsam in the subtropical gyres. Geophysical Research Letters 43 (23), 12,228–12,233.

Beron-Vera, F. J., Olascoaga, M. J., Miron, P., 2019. Building a maxey-riley framework for surface ocean inertial particle dynamics. Physics of Fluids 31 (29).

Beron-Vera, F. J., Olascoaga, M. J., Putman, N. F., Triñanes, J., Goni, G., Lumpkin, R., 2022. Dynamical geography and transition paths of Sargassum in the tropical Atlantic. AIP advances 12 (10).

Buffoni, G., Falco, P., Griffa, A., Zambianchi, E., 1997. Dispersion processes and residence times

in a semi-enclosed basin with recirculating gyres: An application to the Tyrrhenian Sea. Journal of Geophysical Research: Oceans 102 (C8), 18699–18713.

Cózar, A., Echevarría, F., González-Gordillo, J. I., Irigoien, X., Úbeda, B., et al., 2014. Plastic debris in the open ocean. Proc. Nat. Acad. Sci. 111 (28), 10239–10244.

Csanady, G. T., 2012. Turbulent diffusion in the environment. Vol. 3. Springer Science & Business Media.

Cushman-Roisin, B., Beckers, J.-M., 2009. Introduction to Geophysical Fluid Dynamics Physical and Numerical Aspects. Cambridge University Press.

Durán Colmenares, A., Zavala Sansón, L., 2022. Anisotropic Lagrangian dispersion in zonostrophic turbulence in a closed basin. Phys. Fluids 34 (10).

Estrada-Allis, S., Barceló-Llull, B., Pallàs-Sanz, E., Rodríguez-Santana, A., Souza, J., Mason, E., McWilliams, J. C., Sangrà, P., 2019. Vertical velocity dynamics and mixing in an anticyclone near the Canary Islands. Journal of Physical Oceanography 49 (2), 431–451.

Flores Ramírez, L. M., Zavala Sansón, L., 2019. Two-dimensional turbulence dispersion in a closed domain: Influence of confinement and geometry. AIP Advances 9 (3).

Froyland, G., Stuart, R. M., van Sebille, E., 2014. How well-connected is the surface of the global ocean? Chaos: An Interdisciplinary Journal of Nonlinear Science 24 (3).

Graef, F., Zavala Sansón, L., Plata, L., Ochoa, J., 2020. Dispersion of particles in two-dimensional circular vortices. Phys. Fluids 32 (3).

Griffa, A., 1996. Applications of stochastic particle models to oceanographic problems. Stochastic Modelling in Physical Oceanography, 113–140.

Isobe, A., Iwasaki, S., 2022. The fate of missing ocean plastics: Are they just a marine environmental problem? Science of the Total Environment 825, 153935.

Jalón-Rojas, I., Wang, X., Fredj, E., 2019. On the importance of a three-dimensional approach for modelling the transport of neustic microplastics. Oc. Sci. 15 (3), 717–724.

Jambeck, J., Geyer, R., Wilcox, C., Siegler, T., Perryman, et al., 2015. Plastic waste inputs from land into the ocean. Science 347 (6223), 768–771.

Kubota, M., 1994. A mechanism for the accumulation of floating marine debris north of Hawaii. Journal of Physical Oceanography 24 (5), 1059–1064.

Luyten, J., Pedlosky, J., Stommel, H., 1983. The ventilated thermocline. J. Phys. Oceanogr. 13 (2), 292–309.

Maxey, M. R., Riley, J. J., 1983. Equation of motion for a small rigid sphere in a nonuniform flow.

Physics of Fluids 26 (4), 883–889.

Maximenko, N., Hafner, J., Niiler, P., 2012. Pathways of marine debris derived from trajectories of lagrangian drifters. Marine Pollution Bulletin 65 (1-3), 51–62.

McGillicuddy Jr, D. J., 2016. Mechanisms of physical-biological-biogeochemical interaction at the oceanic mesoscale. Ann. Rev. Mar. Sci. 8, 125–159.

Miron, P., Olascoaga, M., Beron-Vera, F., Putman, N., Triñanes, J., Lumpkin, R., Goni, G., 2020. Clustering of marine-debris-and sargassum-like drifters explained by inertial particle dynamics. Geophysical Research Letters 47 (19), e2020GL089874.

Ocampo Jaimes, J., Graef, F., Zavala Sansón, L., 2022. Dispersion of particles in two-dimensional monopolar and dipolar vortices using a lagrangian stochastic model. Physics of Fluids 34 (4).

Olascoaga, M. J., Beron-Vera, F. J., Miron, P., Triñanes, J., Putman, N., Lumpkin, R., Goni, G., 2020. Observation and quantification of inertial effects on the drift of floating objects at the ocean surface. Physics of Fluids 32 (2).

Onink, V., Wichmann, D., Delandmeter, P., van Sebille, E., 2019. The role of Ekman currents, geostrophy, and Stokes drift in the accumulation of floating microplastic. Journal of Geophysical Research: Oceans 124 (3), 1474–1490.

Richards, K. J., Jia, Y., Rogers, C. F., 1995. Dispersion of tracers by ocean gyres. Journal of Physical Oceanography 25 (5), 873–887.

Stommel, H., 1948. The westward intensification of wind-driven ocean currents. Eos, Transactions American Geophysical Union 29 (2), 202–206.

van der Mheen, M., Pattiaratchi, C., van Sebille, E., 2019. Role of indian ocean dynamics on accumulation of buoyant debris. Journal of Geophysical Research: Oceans 124 (4), 2571–2590.

van Sebille, E., England, M. H., Froyland, G., 2012. Origin, dynamics and evolution of ocean garbage patches from observed surface drifters. Environmental Research Letters 7 (4), 044040.

Wichmann, D., Delandmeter, P., van Sebille, E., 2019. Influence of near-surface currents on the global dispersal of marine microplastic. Journal of Geophysical Research: Oceans 124 (8), 6086–6096.

Young, W., 1984. The role of western boundary layers in gyre scale ocean mixing. J. Phys. Oceanogr. 14 (2), 478–483.

Zavala Sansón, L., García-Martínez, I., Sheinbaum, J., 2023. Nonlinear surface Ekman effects on cyclonic and anticyclonic vortices. Journal of Fluid Mechanics 971, A35.

Zavala Sansón, L., Graef, F., Pavia, E., 1998. Collision of anticyclonic, lens-like eddies with a

meridional western boundary. Journal of Geophysical Research: Oceans 103 (C11), 24881–24890.

Zavala Sansón, L., Pérez-Brunius, P., Sheinbaum, J., 2017. Surface relative dispersion in the southwestern Gulf of Mexico. Journal of Physical Oceanography 47 (2), 387–403.

Zhong, Y., Bracco, A., 2013. Submesoscale impacts on horizontal and vertical transport in the Gulf of Mexico. Journal of Geophysical Research: Oceans 118 (10), 5651–5668.

Zhong, Y., Bracco, A., Tian, J., Dong, J., Zhao, W., Zhang, Z., 2017. Observed and simulated submesoscale vertical pump of an anticyclonic eddy in the South China Sea. Scientific Reports 7 (1), 44011.